Rear cortex contraction aids in nuclear transit during confined migration by increasing pressure in the cell posterior

Jeremy Keys[1,2], Brian C.H. Cheung[3], Mingming Wu[3], Jan Lammerding[1,2]

[1]Nancy E. and Peter C. Meinig School of Biomedical Engineering, Cornell University, Ithaca, NY, USA

[2]Weill Institute for Cellular and Molecular Biology, Cornell University, Ithaca, NY, USA

[3]Department of Biological and Environmental Engineering, Cornell University, Ithaca, NY, USA

Correspondence should be addressed to Jan Lammerding: jan.lammerding@cornell.edu

Abstract

As cells migrate through biological tissues, they must frequently squeeze through micron-sized constrictions in the form of interstitial pores between extracellular matrix fibers and/or other cells. Although it is now well recognized that such confined migration is limited by the nucleus, which is the largest and stiffest organelle, it remains incompletely understood how cells apply sufficient force to move their nucleus through small constrictions. Here, we report a novel mechanism by which contraction of the cell rear cortex pushes the nucleus forward to mediate nuclear transit through constrictions. Laser ablation of the rear cortex reveals that pushing forces behind the nucleus are the result of increased intracellular pressure in the rear compartment of the cell. The pushing forces behind the nucleus depend on accumulation of actomyosin in the rear cortex and require Rho-kinase (ROCK) activity. Collectively, our results suggest a novel mechanism by which cells generate elevated, intracellular pressure in the posterior compartment to facilitate nuclear transit through 3D constrictions. This mechanism may supplement or even substitute for other mechanisms supporting nuclear transit, ensuring robust cell migrations in confined 3D environments.

***Key words*:** Nucleus, Confined Migration, Invasion, Cortex, Mechanobiology; Pressure

26 **Introduction**

27 The migration of cells through tissues is essential to many biological processes, including
28 embryogenesis, immune surveillance, wound healing, and cancer metastasis (Doyle et al., 2013;
29 Yamada and Sixt, 2019). During in vivo migration, cells must navigate through extracellular matrix
30 networks and layers of endothelial cells, which form constrictions as small as 1 to 2 μm in diameter
31 (Bone et al., 2016; Khatau et al., 2012; Weigelin et al., 2012; Wolf et al., 2013), i.e., substantially
32 smaller than the size of the cell and the nucleus. Although cells can readily alter their morphology
33 through cytoskeletal reorganization to adjust to the size of the constriction, the deformation of the
34 nucleus represents a unique physical challenge, as it is the largest and stiffest organelle in the
35 cell (Caille et al., 2002; Denais et al., 2016; Khatau et al., 2012; McGregor et al., 2016; Wolf et
36 al., 2013). Because of the size and stiffness of the nucleus, cells must generate substantial
37 intracellular forces to deform the nucleus through the constrictions. The process of deforming and
38 moving the nucleus through these narrow spaces, henceforth referred to as "nuclear transit," limits
39 the rate at which cells migrate in confined 3D environments (Davidson et al., 2015; Denais et al.,
40 2016; Harada et al., 2014; Jayo et al., 2016; McGregor et al., 2016; Rowat et al., 2013; Thomas
41 et al., 2015; Tollis et al., 2022; Wolf et al., 2013; Yadav et al., 2018).
42
43 Various mechanisms have been proposed to explain how cells accomplish nuclear transit through
44 confined environments (Marks and Petrie, 2022; McGregor et al., 2016). One commonly
45 described mechanism suggests that actomyosin and intermediate filaments at the front of the cell
46 pull the nucleus forward (Davidson et al., 2020; Jayo et al., 2016; Petrie et al., 2014). Other studies
47 have implicated pushing forces in the process, mediated through perinuclear actomyosin fibers,
48 which wrap around the nucleus (Thomas et al., 2015), or Arp2/3-mediated perinuclear actin
49 polymerization (Thiam et al. 2016). Each of these mechanisms depend on physical connections
50 between the nucleus and cytoskeleton. Another proposed mechanism suggests that the nucleus

is pushed forward by contraction of actomyosin in the rear cortex of migrating cells (Hetmanski et al., 2019; Lämmermann et al., 2008; Lee et al., 2021; Mistriotis et al., 2019; Poincloux et al., 2011). Support for pushing forces behind the nucleus derives from the observation that cells migrating in 3D environments commonly accumulate actin in the trailing edge of the cell, and that contraction of the cell rear often precedes nuclear transit (Hetmanski et al., 2019; Lämmermann et al., 2008; Mistriotis et al., 2019; Thiam et al., 2016). However, functional evidence for this mechanism is still lacking, including how forces from the contraction of the rear cortex are transmitted to the nucleus. Lastly, many cell lines have shown the ability to migrate using multiple modes, such as adhesion-independent “amoeboid” migration and integrin adhesion-based “mesenchymal” migration, depending on cellular contractility and environmental adhesiveness (Liu et al., 2015; Sahai and Marshall, 2003). This plasticity of migration modes suggests that it is possible that cells may similarly switch between nuclear transit mechanisms in differing biological contexts (Marks and Petrie, 2022), but experimental evidence for this has been lacking. Thus, despite extensive previous research, several questions remain regarding the potential mechanism cells use to apply cytoplasmic forces to the nucleus during confined migration, including (1) how forces are transmitted from the contracting cell rear to the nucleus, and (2) to what extent contraction of the cell rear contributes to or is necessary for nuclear transit through small constrictions. Using microfluidic devices that mimic confined interstitial spaces, along with advanced imaging and cellular manipulation approaches, we here report a novel mechanism by which actomyosin in the rear cortex contracts to push the nucleus forward through constrictions. This mechanism is associated with enrichment of actin and active myosin in the rear cell cortex and depends on elevated RhoA-ROCK signaling. RhoA-ROCK mediated contraction of the rear cortex results in elevated intracellular pressure in the posterior compartment of the cell, which pushes the nucleus from behind to support migration through confined spaces.

76 **Results**

77 ***Contraction of the posterior actin cortex promotes nuclear transit through constrictions***

78 To model cell migration through confined environments, we seeded cells into microfluidic devices
79 that enable the close observation of nuclear transit through precisely defined constrictions at high
80 spatiotemporal resolution (Davidson et al., 2015; Keys et al., 2018). In these devices, cells migrate
81 through collagen-coated channels with constrictions measuring 1 to 2 μm in width and 5 μm in
82 height (cross-sectional area ≤2×5 μm^2), formed by poly-dimethyl siloxane (PDMS) pillars
83 (**Fig. 1A**). The devices also feature wider control channels (15×5 μm^2) that do not require
84 substantial nuclear deformation during migration (**Fig. 1A**) (Davidson et al., 2015). The size of the
85 narrow constrictions reflects the geometries of small pore sizes that migrating cancer cells
86 encounter in vivo (Weigelin et al., 2012), while the width of the control channels was chosen to
87 be wider than the typical diameter of nuclei (Lammerding, 2011) and corresponds to the upper
88 range of interstitial spaces (Weigelin et al., 2012). We have previously demonstrated that the
89 5 μm height is sufficient to vertically confine migrating cells, and that cells adhere to both top and
90 bottom surfaces of the cell, plus the vertical walls (Davidson et al., 2015, 2014), thereby creating
91 true 3D confined environments that model confined migration *in vivo* (Denais et al., 2016; Wang
92 et al., 2022). These devices provide several advantages over imaging cells migrating through
93 collagen matrices, as they enable long-term imaging of cells migrating along a single focal plane,
94 through precisely defined constriction geometries. In contrast, in vitro assembled collagen
95 matrices have heterogeneous, randomly distributed constriction geometries and often lead to cells
96 migrating out of the imaging plane during prolonged image acquisition series.

97

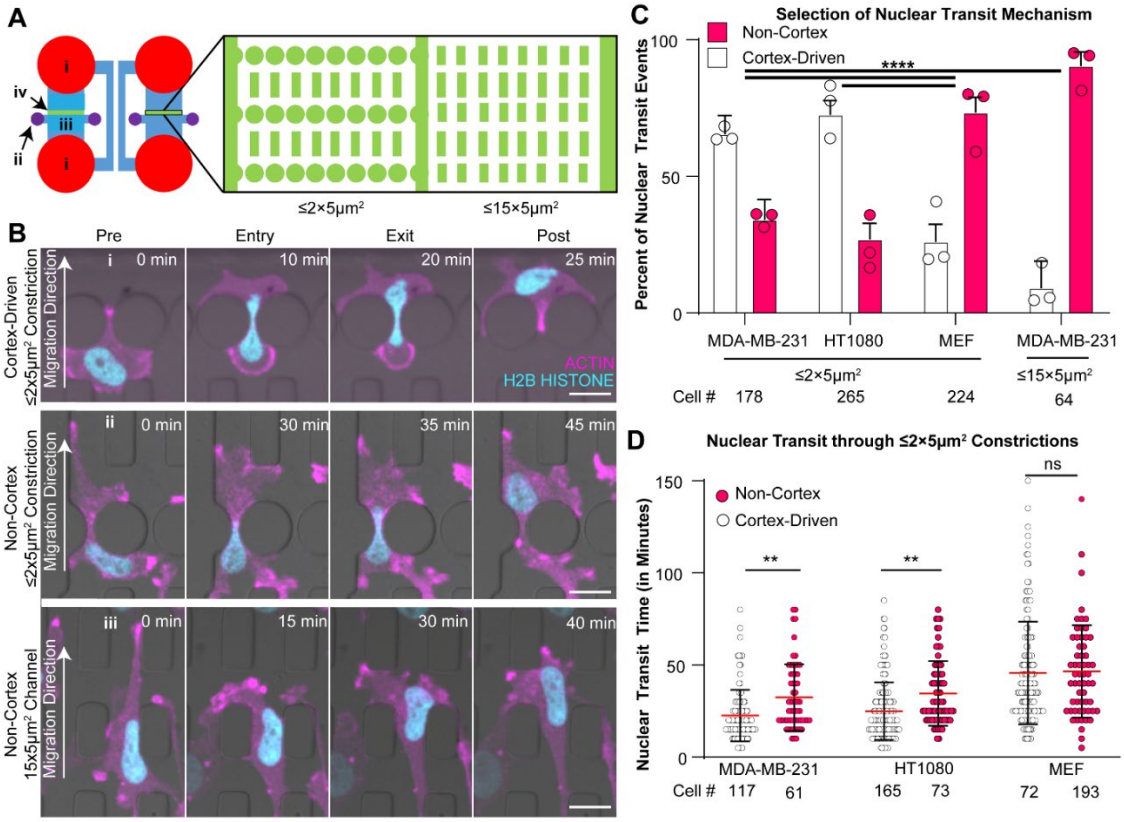

Figure 1. Cortex-driven nuclear transit provides an advantage to cells migrating through narrow constrictions. (**A**) Schematic layout of microfluidic device used to study confined migration through precisely defined constrictions. (i) Reservoirs for cell media; (ii) seeding ports to add cells; (iii) seeding area where cells attach prior to migration through constrictions; (iv) constriction area, shown in detail in inset, to the right. The inset shows areas with constrictions (left) and the larger control channels (right), with the corresponding cross-sections listed below each area. (**B**) Representative image sequences of MDA-MB-231 cells co-expressing fluorescently labeled histones (mNeonGreen-H2B, cyan) and actin (mCherry2-actin chromobody, magenta). MDA-MB-231 cells adopt varying morphological characteristics as the nucleus squeezes through microfluidic constrictions using either (i) a rear cortex-driven mechanism, or (ii) a non-cortex driven mechanism. Scale bar: 20 μm. (**C**) Relative frequency of cortex-driven and nuclear transit mechanisms in varying cell types migrating through either narrow constrictions (≤2×5 μm^2) or wider control channels (15×5 μm^2). Error bars represent 95% confidence intervals. ****, $p < 0.0001$, based on a Chi-Squared test of independence. Circles represent means of experimental replicates. (**D**) Nuclear transit times through ≤2×5 μm^2 constrictions of different cell types, subdivided into cortex-driven and non-cortex

driven nuclear transit mechanisms. Red line represents sample mean. Error bars represent standard deviation. **, $p < 0.01$; ****, $p < 0.0001$, based on one-way ANOVA.

We chose to study MDA-MB-231 metastatic breast cancer cells because they exhibit the ability to switch between different migration modes (Geiger et al., 2019; Sahai and Marshall, 2003) and therefore may use multiple mechanisms to drive nuclear transit. MDA-MB-231 cells stably expressing fluorescently labeled histones (mNeonGreen-H2B Histone (Davidson et al. 2015)) and actin (mCherry2-actin chromobody (Chromotek)) exhibited two distinct patterns of actin accumulation around the nucleus while migrating through constrictions in microfluidic migration devices. Most cells formed a rounded, actin-enriched cortex in the rear of the cell, the contraction of which was associated with the nucleus squeezing through the constriction (**Fig. 1B-i, Supp. Movie 1**). In other cells, the nucleus transited through the constriction without the cell forming a rounded rear cortex (**Fig. 1B-ii**). Notably, whereas the formation of a distinct, rounded rear cortex was observed in the majority of MDA-MB-231 cells migrating through narrow constrictions, it was rarely observed in cells migrating through the larger control channels, nor in cells migrating on 2D glass substrates (**Fig. 1B-iii, 1C, Supp. Fig. S1C**). We observed similar patterns of actin accumulation at the rear of MDA-MB-231 cells migrating through 3-dimensional collagen matrices (**Supp. Fig. S1**). Together with previous observations of the formation of a rounded rear cortex in MDA-MB-231 cells during transendothelial migration (Chen et al. 2016), our results indicate that these nuclear transit mechanisms are relevant during migration in physiological environments.

We hypothesized that the differences in cytoskeletal organization prior to and during nuclear transit indicate two distinct nuclear transit mechanisms, which may correspond with the previously described “pushing” and “pulling” forces. Accumulation of actin in the rear cortex suggests a “cortex-driven” pushing of the nucleus from behind, whereas accumulation of actin in front of the nucleus suggests “non-cortex-driven” pulling at the front of the nucleus. We recorded similar actin

139 dynamics in HT1080 fibrosarcoma cells in microfluidic migration devices (**Fig. 1C, Supp. Fig.**
140 **S2B**), another cancer cell line that shows considerable plasticity in its migratory mode (Petrie et
141 al., 2016; Wolf et al., 2003). In contrast, mouse embryonic fibroblasts (MEFs), which tend to use
142 a mesenchymal migration mode (Gadea et al., 2007), predominantly used a non-cortex driven
143 nuclear transit mode (**Fig. 1C, Supp. Fig. S2A, Supp. Movie 2**).
144
145 Based on these observations, we hypothesized that the rear cortex contraction may aid MDA-
146 MB-231 and HT1080 cells in nuclear transit through narrow constrictions by applying "pushing"
147 forces to the nucleus from the back of the cell. To determine whether the rear cortex contraction
148 produced more rapid nuclear transit, we compared the transit times between cells using either
149 (rear) cortex-driven or non-cortex driven nuclear transit for each of the cell lines. In MDA-MB-231
150 and HT1080 cells, cortex-driven cells translocated their nuclei significantly faster through narrow
151 constrictions than non-cortex-driven cells (**Fig. 1D**), suggesting that in these cell types, the rear
152 cortex contractions provide an advantage over non-cortex driven migration. In contrast, we did
153 not find any differences in nuclear transit time in in MEFs using either the cortex or non-cortex
154 driven mechanism (**Fig. 1D**). The preference towards a cortex-driven mechanism seen in MDA-
155 MB-231 and HT1080 cells, in contrast to MEFs, may be due to the greater migratory plasticity
156 that is commonly observed in these cancer cell lines (Sahai and Marshall, 2003). As MDA-MB-
157 231 and HT1080 cells are capable of migrating using both mesenchymal and amoeboid migration
158 modes, depending on environmental and biological factors, they may be able to use this additional
159 cortex-driven nuclear transit mechanism to support passage through narrow constrictions. MEFs,
160 in contrast, are more conventionally mesenchymal in their migration (Gadea et al. 2007), and
161 therefore may be less able to use this additional migration mechanism. Taken together, these
162 results suggest that rear cortex contraction may act as an alternative or supplemental mechanism
163 in confined migration, which enables more rapid migration through constrictions but is not
164 necessarily required for nuclear transit.

165

166 Since previous studies had suggested that pulling forces at the leading edge of the nucleus
167 require connections between the nucleus and cytoskeleton (Petrie et al. 2014, Davidson et al.
168 2021), we investigated whether disruption of the linker of nucleoskeleton and cytoskeleton (LINC)
169 complex caused a switch to a cortex-driven nuclear transit mechanism. MEFs expressing GFP-
170 Nesprin-2 (Davidson et al. 2021) and mCherry2-Actin chromobody were transfected with a BFP-
171 tagged dominant-negative KASH construct (DN-KASH), which binds with Sun proteins at the
172 nuclear envelope and prevents the association between Sun proteins and endogenous Nesprin
173 proteins, thereby disrupting force transmission between the cytoskeleton and nucleus (Lombardi
174 et al. 2011). Whereas GFP-Nesprin-2 was localized to the nuclear envelope in non-modified cells
175 and in cells expressing a BFP-only control constructs, in DN-KASH expressing MEF cells,
176 Nesprin-2 was mislocalized from the nuclear envelope to the ER (**Supp. Fig. S3A & B)**, confirming
177 disruption of the LINC complex by the DN KASH construct. Surprisingly, LINC complex disruption
178 did not correspond with increased nuclear transit times, nor in a shift towards a cortex-driven
179 mechanism (**Supp. Fig. S3C & D**). These findings suggest that nuclear transit can be
180 accomplished in the absence of the LINC complex, and neither cortex-driven nor non-cortex
181 driven nuclear transit mechanisms require an intact LINC complex.

182

183 ***Pushing forces behind the nucleus are generated by actomyosin contraction in the rear***
184 ***cortex***

185 We hypothesized that cortex-driven cells localize contractile machinery to the rear cortex to push
186 the nucleus through constrictions. Previous studies found that non-muscle myosin II is important
187 for force generation during 3D confined migration (Davidson et al. 2020; Thomas et al. 2015);
188 thus, we performed time lapse video microscopy on MDA-MB-231 cells transfected to transiently
189 express GFP-myosin IIA and mCherry-myosin IIB in the migration devices. Both myosin II
190 isoforms localized to the rear cortex of cells as the nucleus squeezed through constrictions

191 (**Fig. 2A**). Notably, the accumulation of myosin II at the rear cortex was only observed in cells
192 migrating through narrow constrictions, whereas in cells migrating through larger control channels
193 or on 2D surfaces, i.e., in situations not utilizing rear-cortex driven nuclear transit, myosin II was
194 localized to the front of the cell body or the leading edge of the nucleus (**Fig. 2A, Supp. Fig. S4A-**
195 **B**). Importantly, our studies also revealed that individual cells can switch between non-cortex-
196 driven and cortex-driven mechanisms during nuclear transit. In some instances, cells that entered
197 constrictions with GFP-myosin II initially primarily localized at the leading edge of the nucleus
198 failed to pass through constrictions. When the nuclear transit attempt was not successful, the cells
199 backed out of the constriction, and re-entered the constriction with GFP-myosin IIA localized to
200 the rear cortex, using rear cortex contraction to successfully push the nucleus through the
201 constriction (**Supp. Movie 3**). These findings suggest that cells may actively switch between
202 nuclear transit modes while squeezing through small constrictions.
203
204 To map myosin activity, rather than observe only the distribution of myosin, we
205 immunofluorescently labeled cells fixed inside the microfluidic devices for phosphorylated myosin
206 light chain (pMLC), an indicator of active actomyosin contractility. Cells in which the nucleus had
207 just begun to enter the narrow constrictions displayed characteristic pMLC localization at the rear
208 cortex of cells, indicating that the rear cortex actively contracts with the onset of nuclear transit
209 (**Supp. Fig. S4C**). Importantly, the localization of pMLC to the rear cortex was only observed in
210 cells undergoing nuclear transit through narrow constrictions, and was not seen in cells migrating
211 through wider control channels or on 2D substrates, consistent with our prior observations that
212 cells only use the cortex-driven mechanism when encountering small constrictions (**Supp. Fig.**
213 **S4C**). Of note, pMLC was also found at the leading edge of the nucleus, suggesting that cortex-
214 driven cells may also apply complementary pulling forces at the leading edge of the nucleus or
215 that myosin II activity is required for the protrusion and extension of the leading edge (**Supp. Fig.**
216 **S4C**).

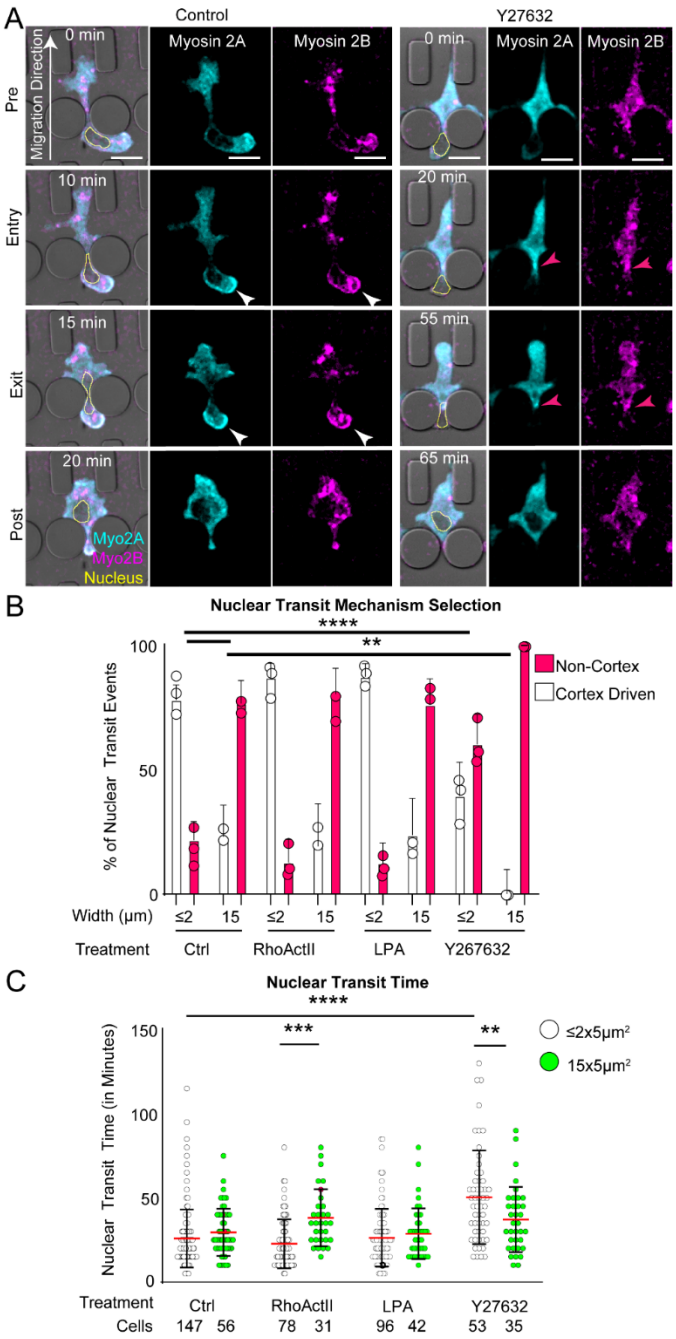

Figure 2: Rear cortex driven nuclear transit is associated with localization of myosin II to the rear cortex. (**A**) Representative time-lapse series of MDA-MB-231 cells expressing GFP-myosin IIA and mCherry-myosin IIB migrating through microfluidic migration devices. White arrows indicate accumulation of myosin II at the rear cortex. Magenta arrows point to accumulation in front of the nucleus. The nucleus is outlined in yellow for better visibility in the merged image. Scale bars: 20 µm (**B**) Percentage of nuclear transit events using cortex-driven or non-cortex driven modes in either ≤2×5µm^2 or 15×5µm^2 constrictions

following treatment with either RhoA activators (RhoActII or LPA), ROCK inhibitor (Y27632), or vehicle control. Error bars represent 95% confidence intervals. **, $p < 0.01$; ****, $p < 0.0001$, based on a Chi-Squared Test of Independence. Circles represent mean of each experimental replicate. (**C**) Nuclear transit times of MDA-MB-231 cells migrating through constrictions following treatment with RhoA activators (RhoActII or LPA) or ROCK inhibitor (Y27632). Red line represents mean. Error bars represent standard deviation. **, $p < 0.01$; ***, $p < 0.001$; ****, $p < 0.0001$, based on a one-way ANOVA. Number of cells in each group indicated below the graphs.

Since myosin contractility is regulated through RhoA and Rho-associated protein kinase (ROCK) (Ridley 2003), we hypothesized that cells locally activate RhoA in the rear cortex to generate actomyosin contractile forces to push the nucleus from behind. To record the spatiotemporal dynamics of RhoA activation during nuclear transit, we stably modified MDA-MB-231 cells with a previously established FRET-based biosensor for RhoA activity (Pertz et al. 2006) and imaged the cells as they migrated through constrictions. Local RhoA activity was determined by measuring the average FRET ratio in either the rear cortex, front cortex, or directly in front of the nucleus (**Supp. Fig. S5A**). Since levels of the RhoA sensor inside the nucleus were very low, as expected, which could negatively affect the robustness of ratiometric FRET analysis, the nucleus was masked-out and excluded from the analysis (**Supp. Fig. S5A**). FRET ratios of the RhoA biosensor were evaluated prior to nuclear transit (“Pre”), during nuclear entry into a constriction (“Entry”), immediately upon nuclear exit from the constriction (“Exit”), and after the cell had left the constriction (“Post”) (**Fig. 3A**). In cells migrating through narrow constrictions, RhoA activity was elevated in the rear cortex relative to the rest of the cell body throughout nuclear transit (**Fig. 3B**). Of note, increased RhoA activity in the rear cortex was unique to cells migrating through narrow 3D constrictions and was not observed in cells migrating through the wider control channels or on 2D substrates (**Supp. Fig. S5B**). In confined conditions, RhoA activity in the rear cortex increased as the nucleus entered the constriction, and then returned to baseline levels

250 during the later stages of nuclear transit (**Fig. 3C**). Unlike RhoA activity at the rear cortex, RhoA
251 activity in the front cortex remained constant throughout nuclear transit (**Supp. Fig. S5D**). RhoA
252 activity in front of the nucleus (**Supp. Fig. S5A, yellow zone**) did not increase upon nuclear entry
253 into the constriction but increased at the end of nuclear transit (**Supp. Fig. S5C**). Collectively,
254 these observations suggest a sequential process in which RhoA is first activated at the posterior
255 of the cell, causing contraction of actomyosin in the rear cortex to push the nucleus into a
256 constriction, followed by activation of RhoA in front of the nucleus to contract actomyosin at the
257 leading edge of the nucleus to pull the nucleus through the constriction.

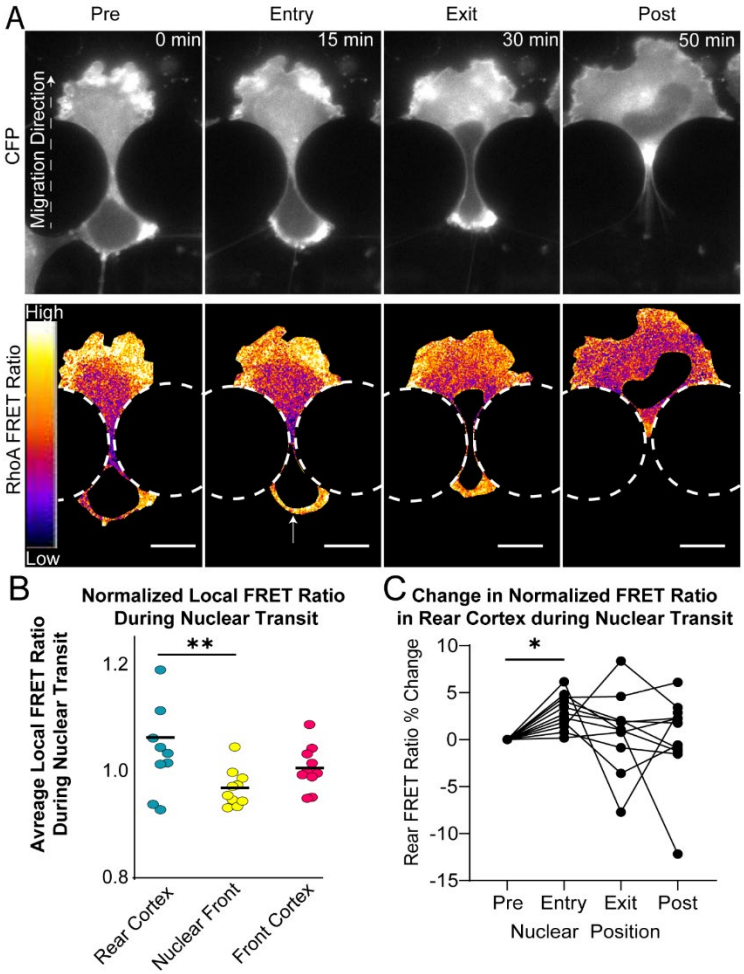

258

259 **Figure 3. Cortex-driven nuclear transit is associated with increased RhoA activity at the rear cortex**.
260 (**A**) Representative time lapse series of FRET ratio of MDA-MB-231 cell expressing RhoA-FRET biosensor
261 migrating through a microfluidic constriction. The bottom series shows the RhoA-FRET ratio during nuclear

262 transit, illustrating increased RhoA activity at the rear cortex (arrow) and the leading edge of the cell. Scale
263 bars: 20 μm (**B**) Comparison of RhoA activity at different intracellular locations based on the recorded RhoA-
264 FRET values for cells migrating through ≤2×5 μm^2 constrictions. Each data point represents local RhoA
265 FRET measurements averaged across all time points during a single nuclear transit event. Black lines
266 represent the mean for each group. **, $p < 0.01$ using paired non-parametric Wilcoxon test. (**C**) Time course
267 of FRET ratio within rear cortex of individual cells (normalized to average FRET ratio of whole cell) at each
268 phase of nuclear transit through ≤2×5μm^2 constrictions. *, $p < 0.05$ using paired non-parametric Wilcoxon
269 test.
270
271 As the cortex-driven nuclear transit mechanism was associated with active RhoA and myosin II
272 at the rear cortex, we hypothesized that the cortex-driven nuclear transit mechanism would
273 depend on Rho-ROCK activity. We treated cells with either ROCK inhibitor (Y27632) or RhoA
274 activators (LPA or RhoA Activator II) and measured nuclear transit times in the microfluidic
275 devices. ROCK inhibitor treatment significantly slowed nuclear transit through the constrictions
276 but did not slow migration through unconfined channels (**Fig. 2C**), suggesting that ROCK activity
277 is particularly important for confined migration. Interestingly, ROCK inhibition increased the
278 frequency of non-cortex driven nuclear transit events and altered localization of myosin IIA and
279 IIB during nuclear transit, causing myosin to localize towards the front of the nucleus, rather than
280 in the rear cortex as is seen in vehicle control cells (**Fig. 2A-B**). As ROCK inhibition slowed down
281 nuclear transit through narrow constrictions but not through unconfined channels, this also
282 suggests that the role of ROCK in pushing the nucleus from behind is unique to nuclear transit
283 through narrow constrictions. This mirrors our earlier observation that cells in unconfined channels
284 rarely use a cortex-driven migration mode. Ectopic activation of RhoA with either LPA or RhoA
285 Activator II had no effect on the nuclear transit rate or nuclear transit mechanism in MDA-MB-231
286 cells (**Fig. 2C**). The lack of effect of pharmacological RhoA activators on nuclear transit rate or
287 mechanism may indicate that RhoA in these cells was already highly activated by FBS in the cell

288 media, or that global RhoA activation without spatial control within the cell is insufficient to activate
289 the cortex-driven transit mechanism. Although actomyosin contractility likely plays a role in both
290 cortex-driven and non-cortex driven mechanisms, these results further suggest that cortex-driven
291 nuclear transit requires a particularly high level of Rho-ROCK mediated contractility in contrast to
292 non-cortex driven nuclear transit.
293
294 ***Laser ablation of the cell cortex reveals a pressure-driven nuclear transit mechanism***
295 Having established that cortex-driven cells localize actomyosin and active RhoA to the rear cortex
296 at the beginning of nuclear transit, we hypothesized that contraction of the rear cortex pressurizes
297 the rear compartment of the cell relative to the front compartment, pushing the nucleus forward
298 through the constriction. To probe differences in intracellular pressure generated by rear cortex
299 contraction, we used a two-photon laser to ablate specific cytoskeletal regions of migrating cells
300 while they squeezed their nucleus through microfluidic constrictions (**Fig. 4A).** As the nucleus
301 transits through a constriction, the cytoskeletal forces pushing or pulling on the nucleus are
302 counteracted by the resistance of the constriction in the form of the friction and the normal forces
303 at the interface between the nucleus and the constriction (**Supp. Fig. S6B-C**).
304
305 Targets for laser ablation were selected based on previously hypothesized roles in applying
306 pushing or pulling forces on the nucleus during nuclear transit, including: (i) perinuclear actin
307 filaments at the leading edge of the nucleus ("Nuclear Front"), which pull the nucleus forward, (ii)
308 the rear cortex, whose contraction pushes the nucleus from behind ("Rear"), (iii) the front cortex
309 at the leading edge of the cell, which may retain pressure in the front compartment of the cell that
310 could inhibit nuclear transit ("Front"), (iv) both cortexes simultaneously to compare
311 compartmentalized pressure in the front and rear of the cell body ("Both"), and (v) non-ablated
312 cells to control for spontaneous movement of the nucleus during experiments (**Fig. 4A**). If
313 contraction of the rear cortex pushes the nucleus forward, then ablation of the rear cortex during

314 nuclear transit is expected to result in the nucleus falling backwards (**Supp. Fig. S6C**). On the
315 other hand, if the nucleus is pulled forward by actomyosin fibers at the leading edge of the
316 nucleus, as has been previously shown in MEFs (Davidson et al. 2020), then ablation at the
317 nuclear front should result in the nucleus moving backwards (**Supp. Fig. 6C**). In contrast, ablation
318 of the front cortex, which may inhibit forward movement of the nucleus through maintaining
319 increased pressure in the front compartment of the cell (Petrie et al. 2014), is expected to result
320 in forward movement of the nucleus (**Supp. Fig. S6C**). In all cases, movement of the nucleus in
321 response to laser ablation is expected to occur almost instantaneously, as ablation should
322 immediately disrupt the balance of forces acting on the nucleus, and nuclear movement will only
323 be resisted by viscous forces within the cytoplasm (in the case of rearward movement) or the
324 resistance of microfluidic constrictions (in the case of forward movement).
325
326 As seen in previous studies (Charras et al. 2005; Mistriotis et al. 2019; Tinevez et al. 2009),
327 ablation of the cell cortex caused the formation of a large plasma membrane bleb, indicating the
328 release of cytosolic pressure (**Fig. 4B, Arrow**). Ablation of the rear cortex and formation of the
329 bleb at the cell posterior led to transient rearward movement of the cell nucleus (**Fig. 4B-D**). This
330 observation supports our hypothesis that contraction of the rear cortex pushes the nucleus from
331 behind by increasing intracellular pressure in the rear compartment. Furthermore, recovery and
332 contraction of the bleb within a minute of the initial laser ablation resulted in forward movement of
333 the nucleus (**Fig. 4B-D**), indicating that restoration of the cell rear cortex increased intracellular
334 pressure in the back of the cell and pushed the nucleus forward.
335
336 Following ablation of the front cortex of cells, the nucleus moved forwards, suggesting that prior
337 to ablation, pressure in the front compartment of the cell impeded forward movement of the
338 nucleus (**Fig. 4C-D, Supp. Fig. S6A**). However, the magnitude of the nuclear forward movement
339 was less than the rearward movement observed when ablating the rear cortex, suggesting that

340 pressure in the rear compartment may be greater than the pressure in the front compartment
341 (**Fig. 4C-D**). To directly assess whether the pressure is greater in the rear compartment of the
342 cell than in the front compartment, we ablated both front and rear cortexes of the cell
343 simultaneously **Fig. 4C-D**). Ablation of both cortexes led to a rearward shift of the nucleus,
344 confirming that the pushing force generated by the pressure from the rear cortex contraction was
345 greater than the resisting force generated by pressure from the front compartment (**Fig. 4C-D**).
346

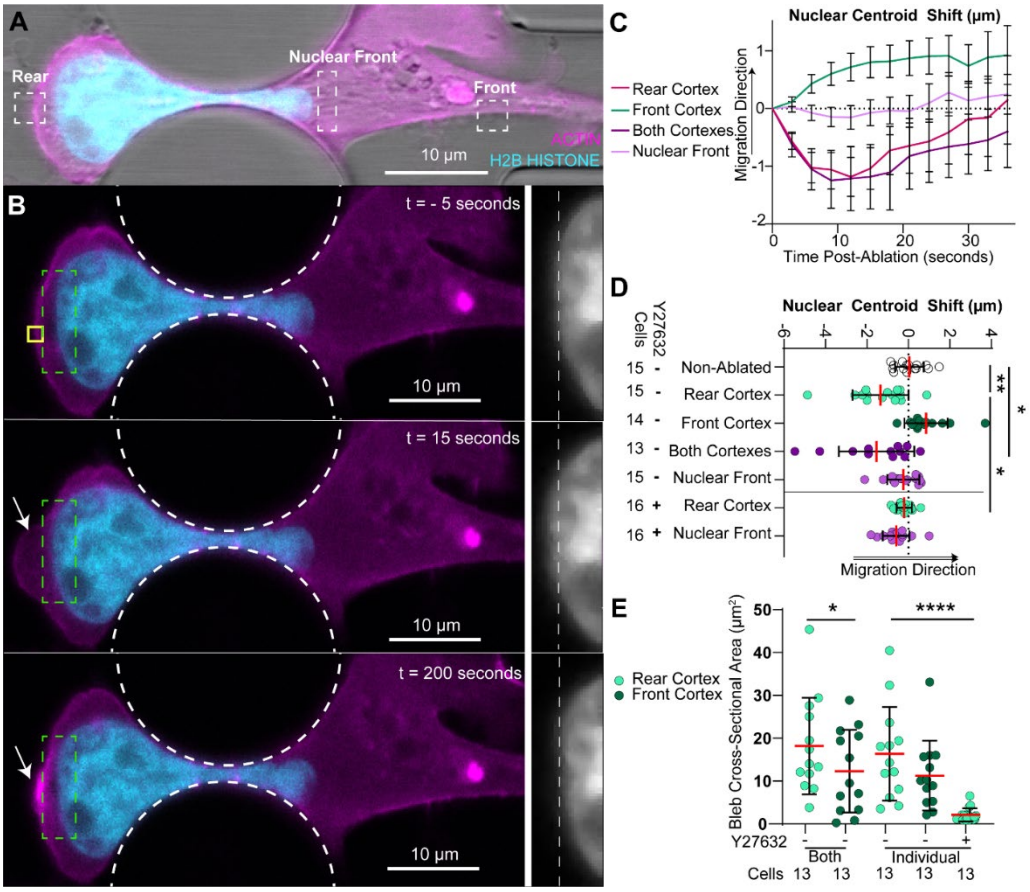

347

348 **Figure 4. Nuclear movement following laser ablation of local actin cytoskeleton reveals that cortex-**
349 **driven nuclear transit results from increased pressure in the rear compartment**. (**A**) Laser ablation
350 set-up. Dashed boxes represent regions targeted for laser ablation in cells starting to undergo nuclear
351 transit through a small (≤2×5 μm^2) constriction. Cells were modified to stably express mNeonGreen-H2B
352 and mCherry actin-chromobody to visualize nuclear movement and actin cytoskeleton, respectively. (**B**)

353 Representative time lapse series of cell ablated at the rear cortex. Yellow box represents laser ablation
354 target. Arrow shows plasma membrane bleb formation post-ablation. Dashed green box corresponds with
355 inlay of mNeonGreen-H2B Histone signal on right. In inlay region: dashed white line represents starting
356 point of leading edge of nucleus. (**C**) Trace of nuclear centroid shift following laser ablation. Error bars
357 represents mean ± SEM, based on 13-16 cells per condition. (**D**) Quantification of peak nuclear centroid
358 shift immediately following nuclear ablation. Red line represents mean, black error bars represent standard
359 deviation. *, $p < 0.05$; **, $p < 0.01$ based on unpaired non-parametric Kruskal Wallis test. (**E**) Cross-sectional
360 area of blebs formed after cortex ablation. *, $p < 0.05$ for paired non-parametric Wilcoxon test; ****, $p <$
361 0.0001 based on unpaired non-parametric Kruskal-Wallis test. Cell counts per condition shown below
362 graph. Red lines represent mean, black error bars represent standard deviation.
363
364 As an additional means of comparing pressure between the front and rear compartments of the
365 cell, we measured the size of blebs in the cell cortex formed as a result of cortex ablation (**Fig. 4E**).
366 Previous work had demonstrated that bleb size following laser ablation increases as a
367 consequence of elevated intracellular pressure, and is limited only by the elasticity of the cell
368 membrane (Tinevez et al. 2009). Thus, increased bleb sizes following laser ablation indicate
369 increased intracellular pressure prior to ablation. Following simultaneous ablation of the front and
370 rear cortexes, blebs formed in the rear compartment were significantly larger than blebs in the
371 front compartment, indicating that pressure in the rear of the cell is greater than pressure in the
372 front compartment (**Fig. 4E**). Collectively, these findings confirm that increased pressure at the
373 cell rear helps to push the nucleus forward through constrictions.
374
375 Ablation directly in front of the nucleus led to a subtle rearward shift of the nucleus, suggesting
376 the presence of pulling forces at the leading edge of the nucleus (**Fig. 4 B-C, Supp. Fig. S6A**),
377 consistent with previous findings (Davidson et al. 2020). However, the rearward movement of the
378 nucleus was very modest in comparison to the movement following rear cortex ablation (**Fig. 4D**).

379 These findings indicate that the cortex-driven cells may rely more heavily on pushing forces from
380 behind the nucleus, than on pulling forces at the nuclear front, which is also consistent with the
381 faster nuclear transit we observed in the cells using the cortex-driven mechanism (**Fig. 1D**).
382
383 We hypothesized that these intracellular pressure-driven pushing forces resulted from the
384 accumulation and contraction of actomyosin in the rear cortex during cortex-driven nuclear transit.
385 As we observed that ROCK-inhibition reduced myosin accumulation in the rear cortex, we
386 hypothesized that ROCK inhibition would reduce intracellular pressure behind the nucleus.
387 Following Y27632 treatment, nuclear movement following rear cortex ablation was reduced,
388 whereas nuclear shift in response to ablation of the nuclear front was unaffected (**Fig. 4D**),
389 indicating that pushing forces between the rear cortex and nucleus result from ROCK-dependent
390 actomyosin contractility. Additionally, ROCK inhibition led to a substantial decrease in the size of
391 blebs formed following laser ablation (**Fig. 4E**), further confirming that ROCK mediated
392 actomyosin contractility drives contraction of the rear cortex and increased cytosolic pressure in
393 the rear compartment of the cell.
394

395 ## Discussion

396 In this study, we investigated the cytoskeletal dynamics and intracellular forces acting on the
397 nucleus as cells migrate through confined spaces. We identified a novel mechanism by which
398 contraction of actomyosin at the rear cortex pushes the nucleus through constrictions during 3D
399 migration. Our results suggest that cortex-driven nuclear transit is a distinct mechanism from
400 alternative “non-cortex-driven” mechanisms, which have been described previously (Davidson et
401 al. 2020; Petrie et al. 2014). In the cortex-driven nuclear transit mechanism, pushing forces at the
402 cell rear are generated through contraction of actomyosin in the posterior cortex, which elevates
403 cytosolic pressure behind the nucleus to push the nucleus forwards (**Fig. 5**). This contrasts the

404 “non-cortex-driven” modes, in which pulling forces, through actomyosin or intermediate filaments,
405 are mediated through physical connections between the nucleus and cytoskeleton (Davidson et
406 al., 2020; Petrie et al., 2014; Thomas et al., 2015) (**Fig. 5**). Our studies suggest that some cell
407 lines are able to use both mechanisms to achieve nuclear transit, though individual cell lines may
408 have a propensity to use one mechanism over another. It remains to be elucidated whether these
409 pushing and pulling mechanisms work independently to accomplish nuclear transit, or whether
410 they act complimentarily.
411

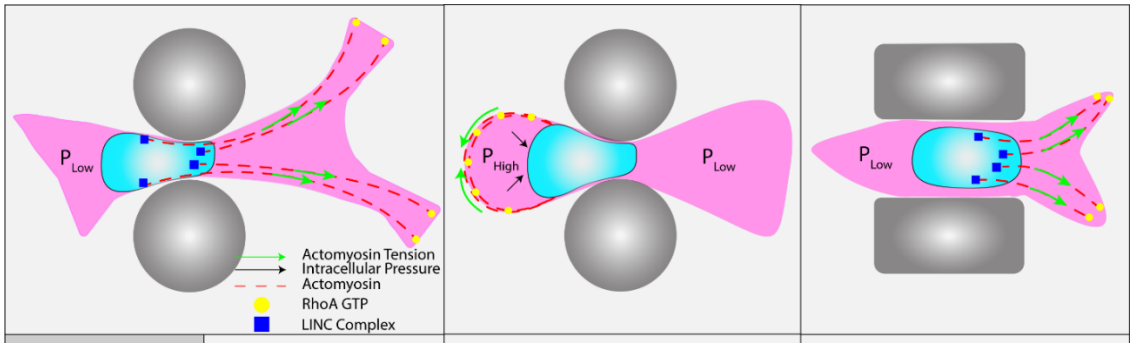

Mechanism	Non-Cortex Driven Confined	**Cortex-Driven Nuclear Transit**	Non-Cortex Driven Unconfined
Environment	3D Confined	**3D Confined**	3D Unconfined
Rho-ROCK Contractility	Low	**High**	Unaffected
Cell Lines	MEF	**MDA-MB-231 & HT1080**	MDA-MB-231, HT1080, & MEF

412
413 **Figure 5: Model of alternate mechanisms of nuclear transit through constrictions**. Pushing forces are
414 generated through contraction of the posterior cortex, caused by co-localization of active RhoA, Myosin II,
415 and Actin. Co-localization of these same proteins at the leading edge of the nucleus can generate pulling
416 forces at the front of the nucleus, mediated through the LINC complex.
417

418 Mirroring our findings in microfluidic devices and collagen matrices, accumulation of actomyosin
419 in the rear of cells migrating in 3D has been observed in MDA-MB-231 cells invading through
420 Matrigel (Poincloux et al., 2011) and in vitro models of transendothelial migration (Chen et al.
421 2016), indicating that cortex-driven nuclear transit may play an important role in these
422 physiological processes. Earlier studies of 3D dendritic cell migration reported that retraction of

423 the cell rear preceded nuclear squeezing through constrictions (Lämmermann et al., 2008). These
424 studies showed that inhibition of contractility through treatment with blebbistatin and Y27632
425 delayed contraction of the cell posterior, which corresponded with a reduced migration rate in
426 confined environments (Lämmermann et al., 2008; Schaar and McConnell, 2005). However, it
427 was unclear whether this retraction represented a direct transmission of force between the rear
428 cortex and the nucleus, or whether rear retraction followed the forward movement of the nucleus.
429 More recent findings have found elevated RhoA activity and myosin at the rear of cells migrating
430 through 3D channels and showed evidence that this resulted in increased intracellular pressure
431 behind the nucleus (Mistriotis et al., 2019). However, these studies did not address how
432 intracellular pressure could contribute to nuclear transit through constrictions. Our results build
433 upon these prior findings by confirming that retraction of the rear cortex pushes the nucleus
434 forward during nuclear transit, and by demonstrating a functional role for cortex-driven pressure
435 generation in confined 3D migration.
436
437 Our findings complement prior studies which have probed intracellular forces acting on the
438 nucleus during cell migration. One such set of studies evaluated the role of pulling forces at the
439 front of the nucleus, which increase intracellular pressure in the front compartment of fibroblasts
440 and HT1080 cells migrating through 3D environments (Petrie et al., 2016, 2014). In contrast with
441 our work, these studies used a probe to directly measure intracellular pressure in cells migrating
442 through 3D cell-derived matrix. They found that actomyosin and intermediate filaments at the
443 nuclear front pulled the nucleus forward to increase pressure at the leading edge of cells, which
444 generated “lobopodia” to enable invasion through 3D environments. However, subsequent
445 studies in mesenchymal stem cells migrating in 3D alginate hydrogels have indicated that pulling
446 forces at the leading edge of the nucleus are not necessary for the formation of lobopodia (Lee et
447 al., 2021). In the absence of nesprins, the nucleus was still able to move forward into constrictions
448 to pressurize the front compartment of cells, while the authors noted an accumulation of pMLC in

449 the rear cortex. These results mirror our findings of active RhoA and pMLC in the rear cortex
450 during nuclear entry to constrictions, supporting the idea that elevated pressure at the cell rear is
451 increased at the beginning of nuclear transit.
452
453 One limitation of our studies is that our detection of intracellular forces must be inferred from
454 protein localization and changes in nuclear position following laser ablation, rather than measuring
455 these forces directly, as the PDMS enclosure of the microfluidic migration devices prevents direct
456 access to the migrating cells. Our laser ablation assay is limited as an indirect measurement of
457 intracellular pressure (or other cytoskeletal forces), as it only reveals forces acting on the nucleus
458 at a single point in time, though the pressure throughout the cell body during nuclear transit may
459 be highly dynamic as the nucleus shifts from the rear compartment of the cell to the front
460 compartment. Additionally, the laser ablation likely disrupts not only actomyosin but also other
461 force-generating cytoskeletal structures within the target region, including intermediate filaments
462 and microtubules, which could further contribute to the force transmission and force generation.
463 Nonetheless, as we found that the cortex-driven mechanism strongly depends on the Rho-ROCK-
464 myosin pathway, we believe that this mechanism principally depends on actomyosin activity,
465 though our results cannot rule out potential contributions of other cytoskeletal elements, which
466 have previously been implicated in nuclear movement (Petrie et al., 2014; Tsai et al., 2010). In
467 addition, the distinct circular shape of rear cortex, in contrast with that of front cortex, further
468 supports the conclusion that the pressure is higher in the rear compartment.
469
470 A recent report demonstrated the role of pulling forces in mediating nuclear transit in MEFs
471 (Davidson et al., 2020). Similar to our results in MDA-MB-231 cells, the authors demonstrated
472 that ROCK inhibition increases nuclear transit times of MEFs migrating through narrow
473 constrictions, but not through unconfined 3D channels (Davidson et al., 2020). Using a laser
474 ablation assay, as we have used here, they found that ablation in front of the nucleus caused a

475 rearward shift in the nucleus whereas ablation at the cell rear had no effect on nuclear movement.
476 They also found that the rearward shift in nuclear position following ablation at the nuclear front
477 was dependent on connections between the nucleus and cytoskeleton. These results contrast
478 with our own using MDA-MB-231 cells, as we detected only very subtle nuclear shifts following
479 ablation of the nuclear front, a significant rearward shift of the nucleus after rear cortex ablation,
480 and LINC complex disruption did not impede nuclear transit (**Supp. Fig. S3**). This difference in
481 results could be attributable to our findings that MEFs scarcely use the cortex-driven nuclear
482 transit mechanism in comparison to MDA-MB-231s, which very frequently used the cortex-driven
483 mode. These two findings are complementary in that they highlight a key difference between
484 MEFs, which in the "non-cortex-driven" mode apply pulling forces at the front of the nucleus
485 (Davidson et al., 2020), and cortex-driven MDA-MB-231 cells which push the nucleus from behind
486 through intracellular pressure generated by the rear cortex.
487
488 Although we have noted a cell-type specific preference towards the cortex-driven mechanism,
489 and that the mechanism depends on high Rho-ROCK-mediated contractility, it remains unclear
490 what biological or environmental factors cause individual cells to adopt a particular nuclear transit
491 mechanism. As others have found that pulling forces at the front of the nucleus depend on the
492 LINC complex (Davidson et al., 2014; Petrie et al., 2016), it is possible that the cortex-driven
493 mechanism could compensate for a lack of pulling forces in specific scenarios. For example,
494 pulling forces at the leading edge of the cell require adhesions to the surrounding environment.
495 Thus, cells that migrate in an adhesion-independent "amoeboid" migration mode may require
496 cortex-driven forces for nuclear transit through narrow constrictions, or cells may benefit from an
497 additional 'boost' from the cortex-driven pressure when pulling forces are insufficient to move the
498 nucleus through a constriction. Surprisingly, in our studies using a dominant negative nesprin
499 construct (DN KASH), we found that LINC complex disruption did not alter nuclear transit time nor
500 nuclear transit mode. Future studies will be necessary to determine the specific factors

501 determining the selection of a particular migration mechanism, and whether this is an active
502 decision-making process requiring specific signaling pathways, or whether cells use multiple
503 migration modes in parallel, with a specific mode dominating depending on the particular
504 microenvironment (Liu et al., 2015; Wolf et al., 2013; Friedl and Wolf, 2010; Geum et al., 2016).
505
506 In discovering this novel mechanism for cortex-driven nuclear transit, we have opened a number
507 of prospective avenues that will improve the understanding of how cells traverse confining 3D
508 environments. An improved understanding of the diverse mechanisms cells have available to
509 overcome narrow interstitial spaces and how cells select between these mechanisms may lead
510 to new targets for therapies to reduce or prevent cancer cell invasion and metastasis, or to boost
511 the migration of immune cells to sites of infection.
512

513 **Methods**

514 ***Cell Culture***

515 MDA-MB-231 metastatic breast adenocarcinoma cells were purchased from American Type
516 Culture Collection (ATCC); HT1080 fibrosarcoma cells were a gift from Peter Friedl and Katarina
517 Wolf, originally purchased from DSMZ in Braunschweig, Germany; MEFs expressing GFP-
518 Nesprin-2 were a gift from Cecile Sykes; MDA-MB-231 cells expressing the RhoA-FRET
519 biosensor were a gift from Louis Hodgson. All cell lines were cultured in Dulbecco's Modified
520 Eagle Medium (DMEM) supplemented with 10% (v/v) fetal bovine serum (FBS, Seradigm VWR),
521 and penicillin and streptomycin (50 U/mL, ThermoFisher Scientific) and were maintained at 37°C
522 and 5% CO2. Cell lines were modified to express fluorescently tagged proteins using lentiviral
523 vectors (pCDH-mCherry2-Actin Chromobody-puro and pCDH-mNeonGreen-H2B Histone-puro).
524 Transient expression of CMV-GFP-NMHC-IIA (Addgene #11347) and mCherry-MyosinIIB-N-18
525 (Addgene #55107) was achieved using a Nucleofector II electroporator and the Cell Line

526 Nucleofector Kit V (Lonza Biosciences). MEF were modified using BFP and DN-KASH expression
527 plasmids in a doxycycline-inducible Piggybac plasmid backbone (Addgene #187019). Cell lines
528 were tested for mycoplasma infection following completion of experiments. Human cell lines were
529 verified through the ATCC Cell Line Authentication Service.
530
531 ***Viral and Piggybac Modification***
532 Pseudoviral particles were produced using 293TN cells (System Biosciences, SBI) were
533 transfected with the lentiviral plasmid of interest as well as lentiviral packaging and envelope
534 plasmids (psPAX and pMD2.G, gifts from Didier Trono) using PureFection transfection reagent
535 (SBI), per manufacturer's protocol. Supernatants were collected at 48, 72, and 96 hour intervals
536 post-transfection and were passed through a 0.45 µm filter. Cells to be transduced were cultured
537 for 24 hours prior to transduction at a confluency of 50% and were then cultured in lentivirus-
538 containing media with polybrene (8 µg/mL). Lentivirus containing media was removed after 24
539 hours, and following an additional 24 hours of recovery time, cells were selected using 1 µg/mL
540 of puromycin (Invivogen) for 3 days. For Piggybac modifications, MEFs were seeded into 6-well
541 plates and were transfected with 1.75 µg of Piggybac plasmids and 0.75 µg of a hyperactive
542 transposase using PureFection Transfection reagent (SBI), per manufacturer's protocol.
543 Transfected cells were selected using 800 µg/mL G418 for 3 days. Cells were sorted using flow
544 assisted cell sorting (FACS) in order to obtain consistent expression levels.
545
546 ***Microfluidic Device Preparation***
547 Microfluidic devices were prepared as previously described (Davidson et al., 2015; Keys et al.,
548 2018). Briefly, microfluidic devices were made through soft lithography by curing
549 polydimethylsiloxane (PDMS) in a plastic mold containing microfluidic features at 65°C for 2
550 hours. After removing cured PDMS from the mold, PDMS features were cut out using biopsy
551 punches, and then both PDMS devices and glass coverslips were washed with deionized water

552 and isopropyl alcohol, and then treated in a plasma cleaner (Harrick Plasma) for 5 minutes. PDMS
553 pieces were then bound to activated coverslips and then heated at 95°C on a hotplate for 1 minute
554 to improve adhesion. After heating, devices were filled with 70% ethanol to sterilize internal
555 surfaces, rinsed with PBS, and then coated with extracellular matrix proteins. For MDA-MB-231
556 cells, devices were coated with 50 µg/mL type-I rat tail collagen (Corning) in 0.02 N glacial acetic
557 acid overnight at 4°C. For MEFs and HT1080 cells, devices were coated with 50 µg/mL fibronectin
558 (Millipore) in PBS overnight at 4°C. Before seeding with cells, devices were rinsed once with PBS
559 and once with cell media. Devices were then aspirated of all media, and then loaded with cell-
560 containing solution (roughly 20,000-30,000 cells per chamber). In devices, cells were cultured in
561 Fluorobrite DMEM supplemented with 10% FBS (Seradigm, VWR), penn/strep (50 U/mL,
562 ThermoFisher), GlutaMAX, and 10 mM HEPES (Gibco). Cells were allowed to attach within
563 devices for 8-12 hours before live cell imaging. Cells were imaged for 12-14 hours at 3-to-5-minute
564 intervals on a Zeiss LSM700 laser scanning confocal microscope at 37°C.
565

566 ***Collagen Matrix Cell Migration Assay***

567 Collagen matrix cell migration assays were performed as previously described (Cross et al.,
568 2010). In brief, PDMS wells were formed by punching out 10 mm diameter holes from PDMS
569 slices. PDMS and glass coverslips were treated in a plasma cleaner for 5 minutes, before bonding
570 PDMS to treated glass slides on a 95°C hot plate for 3 minutes. Wells were coated with 1% PIE
571 for 10 minutes, followed by 0.1% Glutaraldehyde for 30 minutes, and then subsequently washed
572 with PBS once, and cell media once, before adding the collagen solution. Collagen matrices were
573 prepared by mixing Type I rat tail collagen (Corning) with DMEM and NaOH (to reach a neutral
574 pH of 7.4) with a solution of cells suspended in complete DMEM to achieve a final density of
575 80,000 cells/mL. Small volumes of collagen solution (10-15 µL) were pipetted into the middle of
576 wells, where they were allowed to polymerize at 37°C for 30 minutes. Following polymerization,

577 wells were filled with complete DMEM and were subsequently incubated at 37°C for 48 hours
578 before imaging experiments.
579
580 ***Laser Alation of Actin***
581
582 Cells were seeded into migration devices 12-16 hours before ablation experiments. Cells were
583 maintained at 37°C in Fluorobrite DMEM containing 10% FBS, 10 mM HEPES (Gibco), GlutaMax,
584 and penicillin and streptomycin (50 U/mL). Cells were imaged through a water immersion 40×/NA
585 1.1 objective (Carl Zeiss Imaging) using 488-nm and 561-nm laser lines. Cells were imaged at 3
586 second intervals for 63 frames. After 9 seconds, cells were ablated in defined regions using a 780
587 nm laser produced by a Spectra Physics Insight multiphoton excitation source. Ablation was
588 performed at 40-70% attenuation, following ablation tests at the beginning of each experiment to
589 verify that the laser successfully disrupted the actin cytoskeleton without causing cell death. Cells
590 which exited the constriction, displayed rapid blebbing, or appeared to die following laser ablation
591 were excluded from analysis, while cells which were able to recover following disruption of the
592 actin network were included.
593
594 ***Image Analysis of Laser Ablation Experiments***
595 Tracking of nuclear movement following laser ablation was achieved using ImageJ/FIJI software
596 and a custom MATLAB script. Briefly, the image channel containing the fluorescent mNeonGreen-
597 H2B Histone signal was processed using a 3-pixel median filter to eliminate noise, and then a
598 binary mask of this signal was generated using ImageJ/FIJI's built-in RenyiEntropy masking
599 function. This binary mask was then processed in MATLAB to track the position of the nucleus'
600 centroid at each time point. The furthest position of nuclear movement prior to recovery (within 20
601 seconds of the initial ablation) was considered as the direct result of force disruption as a
602 consequence of laser ablation and was recorded as the peak centroid shift (**Supp. Fig. S6D**).
603 Bleb area measurements were performed in ImageJ/FIJI at the time point when the bleb had

604 reached its maximum size. Outer bleb perimeter was traced manually, and inner bleb perimeter
605 was traced at the periphery of the cell at the time point immediately prior to laser ablation.
606
607 ***RhoA FRET Imaging and Analysis***
608 Analysis of RhoA-FRET biosensors was performed as described previously (Cheung et al., 2022).
609 Cells were imaged at regular intervals on a dual channel image acquisition set-up to minimize
610 temporal and spatial misalignment problems which impair FRET result interpretation. Cells were
611 imaged at 5-minute intervals for 12 to 16 hours. Cells were excited with a ET436/20× (CFP
612 Excitation) source for an exposure time of 3 seconds with CFP excitation while CFP and YFP
613 ("FRET") emission channels were captured simultaneously, by using a W-View Gemini beam
614 splitter (A12801-01, Hamamatsu Photonics) and a T505lpxr dichroic mirror, through ET480/40m
615 and ET535/30m optical filters, respectively. The light source for fluorescence imaging was a
616 xenon arc lamp (Lambda LB-LS/30, Sutter Instruments). An absorptive neutral density filter with
617 OD = 0.3 (NE03B-A, ThorLabs) was used to attenuate light to minimize phototoxicity. All filters
618 and dichroic mirrors were purchased from Chroma Technology. Prior to each experiment, the x-
619 y positions of CFP and FRET channels were adjusted using the W-VIEW Adjustment software
620 (Hamamatsu Photonics) to achieve a reasonable alignment for easier image registration and
621 processing. The epifluorescence microscope was surrounded by an incubator with a temperature
622 of 37°C, 5% CO_2, and humidity of ~70%.
623
624 Field alignment, flatfield correction, and background subtraction were performed as described
625 previously (Cheung et al., 2022). Images of cells were then manually masked by tracing the
626 outline of cells using the CFP channel in FIJI/ImageJ. Following these corrections to both the CFP
627 and FRET channels, FRET ratios were calculated by dividing the FRET channel by the CFP
628 channel. The sensitivity of the RhoA-FRET biosensor expressed in this MDA-MB-231 cell line to
629 RhoA activation and inactivation was performed under identical experimental conditions on this

630 imaging set-up as described previously (Cheung et al., 2022). Local FRET ratios were then
631 calculated by manually tracing regions as defined in Supp. Fig. S5A.
632
633 ***Analysis of Migration Mode and Nuclear Transit Times***
634 Measurements of nuclear transit times were performed as described previously (Davidson et al.,
635 2015). Briefly, cells were imaged at 5-minute intervals on a Zeiss LSM710 laser scanning confocal
636 microscope using 488-nm and 561-nm laser lines as they migrated through migration devices
637 over a period of 12-16 hours. A fluorescent marker of the nucleus (either mNeonGreen-H2B
638 Histone, or GFP-Nesprin2) was used to track the position of the nucleus relative to microfluidic
639 constrictions. An imaginary line 5 microns was marked on either side of the middle of the
640 constriction, to define when the nucleus “enters” and “exits” the constriction. The times at which
641 the nucleus enters and passes through the constriction were noted, and this interval was recorded
642 as the nuclear transit time. Cells which did not complete nuclear transit following entry to the
643 constriction were excluded from analysis.
644
645 ***Immunofluorescence Imaging***
646 Cells were fixed in PDMS microfluidic devices using a solution of 4% Paraformaldehyde on ice
647 for 10 minutes, washed twice with PBS for 5 minutes, permeabilized with 0.2% Triton in PBS at
648 room temperature, blocked with a solution of Bovine Serum Albumin (3% v/v) with 0.05% Tween
649 and 0.2% Triton in PBS for 1 hour, and then treated with primary antibodies (anti-pMLC, cell
650 signaling 1:100) in blocking solution overnight at 4°C. Cells were then washed 3 times with PBS
651 for 10 minutes each, and then treated with Secondary Antibodies (Alexa Fluor 488 anti-Rabbit),
652 Phalloidin 647 (1:400 dilution), and Hoechst (1:5000 dilution) for 2 hours at room temperature.
653 Cells were washed 3 times with PBS for 10 minutes each. Devices were filled with blocking
654 solution and sealed with glass coverslips prior to imaging.
655

656 ***Statistical Analysis***

657 All experimental data are based on at least three independent experiments, unless otherwise
658 specified. Statistics tests were performed and graphs were created using GraphPad Prism
659 (GraphPad Software, San Diego, USA). Nuclear transit times were compared using a one-way
660 ANOVA. Frequency of nuclear transit mechanism selection was performed using a Chi Squared
661 test of independence. Changes in local FRET ratio during nuclear transit were evaluated using a
662 paired non-parametric ANOVA test (Wilcoxon). Nuclear centroid shifts following laser ablation
663 were compared using an unpaired non-parametric ANOVA test (Kruskal-Wallis). Bleb formation
664 in cells ablated at a single site were compared using an unpaired non-parametric ANOVA test
665 (Kruskal-Wallis) while bleb formation in cells ablated at both cortexes simultaneously were
666 compared using a paired non-parametric ANOVA test (Wilcoxon).

667

668

669 **Acknowledgements**

670 We thank Louis Hodgson for providing the MDA-MB-231 cell line expressing the RhoA-FRET
671 Biosensor and Peter Friedl and Katarina Wolf for providing the HT1080 fibrosarcoma cell line.
672 The mouse embryonic fibroblast cell line expressing Nesprin-2 GFP was made by Aude Battistella
673 and Patricia Davidson and was a kind gift from Cécile Sykes and Sirine Amiri. We thank Klaus
674 Hahn and Louis Hodgson for their advice regarding the use and analysis of FRET biosensors in
675 migrating cells. We thank Philipp Isermann for his help in setting up the initial laser ablation
676 experiments on MDA-MB-231 cells.

677

678 **Competing Interests**

679 The authors declare no competing interests. Jan Lammerding has received consulting fees from
680 BridgeBio on unrelated projects.

Funding

We acknowledge the support of NYSTEM C029155 and NIH S10OD018516 grants and the help of the Cornell Institute of Biotechnology's BRC Imaging Facility (RRID:SCR_021741) for the use of the Zeiss LSM880 inverted confocal microscope, which received funding through NYSTEM C029155 and NIH S10OD018516 awards for the Zeiss LSM880 inverted confocal microscope. We thank the Biotechnology Resource Center Flow Cytometry Facility (RRID:SCR_021740) for help with Flow Assisted Cell Sorting. This work was performed in part at the Cornell NanoScale Science & Technology Facility, a member of the National Nanotechnology Coordinated Infrastructure, which is supported by the National Science Foundation (award NNCI-2025233). This work was supported by awards from the National Institutes of Health (R01 HL082792, R01 GM137605, U54 CA210184 to J.L.,) the Department of Defense Breast Cancer Research Program (Breakthrough Award BC150580 to J.L.), the National Science Foundation (CAREER Award CBET-1254846 and URoL-2022048 to J.L.), the Volkswagen Stiftung (A130142 to J.L.), and the Knight@KIC Engineering Graduate Fellowship (to J.K.). The content of this manuscript is solely the responsibility of the authors and does not necessarily represent the official views of the National Institutes of Health.

References

Bone, C.R., Chang, Y.T., Cain, N.E., Murphy, S.P., Starr, D.A., 2016. Development 143, 4193–4202.

Caille, N., Thoumine, O., Tardy, Y., Meister, J.J., 2002. J Biomech 35, 177–187.

Charras, G.T., Yarrow, J.C., Horton, M.A., Mahadevan, L., Mitchison, T.J., 2005. Nature 435, 365–369.

Cheung, B.C.H., Hodgson, L., Segall, J.E., Wu, M., 2022. Experimental Cell Research 410, 112939.

Cross, V.L., Zheng, Y., Won Choi, N., Verbridge, S.S., Sutermaster, B.A., Bonassar, L.J., Fischbach, C., Stroock, A.D., 2010. Biomaterials 31, 8596–8607.

Davidson, P.M., Battistella, A., Déjardin, T., Betz, T., Plastino, J., Borghi, N., Cadot, B., Sykes, C., 2020. EMBO Rep 21, e49910.

Davidson, P.M., Denais, C., Bakshi, M.C., Lammerding, J., 2014. Cellular and Molecular Bioengineering 7, 293–306.

Davidson, P.M., Sliz, J., Isermann, P., Denais, C.M., Lammerding, J., 2015. Integr Biol 7, 1534–1546.

Denais, C.M., Gilbert, R.M., Isermann, P., McGregor, A.L., te Lindert, M., Weigelin, B., Davidson, P.M., Friedl, P., Wolf, K., Lammerding, J., 2016. Science (1979) 352, 353–358.

Doyle, A.D., Petrie, R.J., Kutys, M.L., Yamada, K.M., 2013. Curr Op Cell Bio 25, 642–649.

Friedl, P., Wolf, K., 2010. Journal of Cell Biology 188. 11-19

Gadea, G., de Toledo, M., Anguille, C., Roux, P., 2007. Journal of Cell Biology 178, 23–30.

Geiger, F., Rüdiger, D., Zahler, S., Engelke, H., 2019. PLoS ONE 14.

Geum, D., Kim, B., Chang, A., Hall, M., Wu. M., 2016. European Physical Journal Plus.

Harada, T., Swift, J., Irianto, J., Shin, J.-W., Spinler, K.R., Athirasala, A., Diegmiller, R., Dingal, P.C.D.P., Ivanovska, I.L., Discher, D.E., 2014. Journal of Cell Biology 204, 669–682.

Hetmanski, J.H.R., de Belly, H., Busnelli, I., Waring, T., Nair, R. v, Sokleva, V., Dobre, O., Cameron, A., Gauthier, N., Lamaze, C., Swift, J., del Campo, A., Starborg, T., Zech, T., Goetz, J.G., Paluch, E.K., Schwartz, J.-M., Caswell, P.T., 2019. Developmental Cell 51, 460-475.e10.

Jayo, A., Malboubi, M., Antoku, S., Chang, W., Ortiz-Zapater, E., Groen, C., Pfisterer, K., Tootle, T., Charras, G., Gundersen, G.G., Parsons, M., 2016. Dev Cell 38, 371–383.

Keys, J., Windsor, A., Lammerding, J., 2018. Assembly and Use of a Microfluidic Device to Study Cell Migration in Confined Environments, in: Gundersen, G.G., Worman, H.J. (Eds.), The LINC Complex: Methods and Protocols. Springer New York, New York, NY, pp. 101–118.

Khatau, S.B., Bloom, R.J., Bajpai, S., Razafsky, D., Zang, S., Giri, A., Wu, P.H., Marchand, J., Celedon, A., Hale, C.M., Sun, S.X., Hodzic, D., Wirtz, D., 2012. Sci Rep 2.

Lammerding, J., 2011. Compr Physiol 1, 783–807.

Lämmermann, T., Bader, B.L., Monkley, S.J., Worbs, T., Wedlich-Söldner, R., Hirsch, K., Keller, M., Förster, R., Critchley, D.R., Fässler, R., Sixt, M., 2008. Nature 453, 51–55.

Lee, H., Alisafaei, F., Adebawale, K., Chang, J., Shenoy, V.B., Chaudhuri, O., 2021. Science Advances 7, eabd4058.

Liu, Y.-J., Le Berre, M., Lautenschlaeger, F., Maiuri, P., Callan-Jones, A., Heuzé, M., Takaki, T., Voituriez, R., Piel, M., 2015. Cell 160, 659–672.

Marks, P.C., Petrie, R.J., 2022. Phys Biol 19.

McGregor, A.L., Hsia, C., Lammerding, J., 2016. Curr Op Cell Bio 40, 32–40.

Mistriotis, P., Wisniewski, E.O., Bera, K., Keys, J., Li, Y., Tuntithavornwat, S., Law, R.A., Perez-Gonzalez, N.A., Erdogmus, E., Zhang, Y., Zhao, R., Sun, S.X., Kalab, P., Lammerding, J., Konstantopoulos, K., 2019. J Cell Biol 218, 4093–4111.

Pertz, O., Hodgson, L., Klemke, R.L., Hahn, K.M., 2006. Nature 440, 1069–1072.

Petrie, R.J., Harlin, H.M., Korsak, L.I.T., Yamada, K.M., 2016. Journal of Cell Biology 216, 93–100.

Petrie, R.J., Koo, H., Yamada, K.M., 2014. Science (1979) 342, 1062–1065.

Poincloux, R., Collin, O., Lizárraga, F., Romao, M., Debray, M., Piel, M., Chavrier, P., 2011. Proceedings of the National Academy of Sciences 108, 1943–1948.

Rowat, A.C., Jaalouk, D.E., Zwerger, M., Ung, W.L., Eydelnant, I.A., Olins, D.E., Olins, A.L., Herrmann, H., Weitz, D.A., Lammerding, J., 2013. Journal of Biological Chemistry 288, 8610–8618.

Sahai, E., Marshall, C.J., 2003. Nat Cell Biol 5, 711–719.

Schaar, B.T., McConnell, S.K., 2005. PNAS 102.

Thiam, H.R., Vargas, P., Carpi, N., Crespo, C.L., Raab, M., Terriac, E., King, M.C., Jacobelli, J., Alberts, A.S., Stradal, T., Lennon-Dumenil, A.M., Piel, M., 2016. Nature Communications 7.

Thomas, D.G., Yenepalli, A., Denais, C.M., Rape, A., Beach, J.R., Wang, Y.-L., Schiemann, W.P., Baskaran, H., Lammerding, J., Egelhoff, T.T., 2015. J Cell Biol 210, 583–594.

Tinevez, J.-Y., Schulze, U., Salbreux, G., Roensch, J., Joanny, J.-F., Paluch, E., 2009. Proceedings of the National Academy of Sciences 106, 18581–18586.

Tollis, S., Rizzotto, A., Pham, N.T., Koivukoski, S., Sivakumar, A., Shave, S., Wildenhain, J., Zuleger, N., Keys, J.T., Culley, J., Zheng, Y., Lammerding, J., Carragher, N.O., Brunton, V.G., Latonen, L., Auer, M., Tyers, M., Schirmer, E.C., 2022. ACS Chemical Biology 17, 680–700.

768 Tsai, J.W., Lian, W.N., Kemal, S., Kriegstein, A.R., Vallee, R.B., 2010. Nature Neuroscience 13,
769 1463–1472.

770 Weigelin, B., Bakker, G.-J., Friedl, P., 2012. IntraVital 1, 32–43.

771 Wolf, Katarina, te Lindert, M., Krause, M., Alexander, S., te Riet, J., Willis, A.L., Hoffman, R.M.,
772 Figdor, C.G., Weiss, S.J., Friedl, P., 2013. Journal of Cell Biology 201, 1069–1084.

773 Wolf, K, te Lindert, M., Krause, M., Alexander, S., te Riet, J., Willis, L.A., Hoffman, R.M., Figdor,
774 C.G., Weiss, S.J., Friedl, P., 2013. J Cell Biol 201, 1069–1084.

775 Wolf, K., Mazo, I., Leung, H., Engelke, K., von Andrian, U.H., Deryugina, E.I., Strongin, A.Y.,
776 Bröcker, E.B., Friedl, P., 2003. Journal of Cell Biology 160, 267–277.

777 Yadav, S.K., Feigelson, S.W., Roncato, F., Antman-Passig, M., Shefi, O., Lammerding, J., Alon,
778 R., 2018. Journal of Leukocyte Biology 104, 239–251.

779 Yamada, K.M., Sixt, M., 2019. Nature Reviews Molecular Cell Biology 20, 738–752.

780

781